research papers

Enhancement of measurement accuracy of X-ray PIV in comparison with the micro-PIV technique

Hanwook Park,[a] Sung Yong Jung,[b] Jun Hong Park,[a] Jun Ho Kim[a] and Sang Joon Lee[a]*

[a]Department of Mechanical Engineering, Pohang University of Science and Technology (POSTECH), 77 Cheongam-ro, Pohang, Gyeongsangbuk-do 790-784, South Korea, and [b]Department of Mechanical Engineering, Chosun University, 375 Seosuk-dong, Dong-gu, Gwangju 61452, South Korea. *Correspondence e-mail: sjlee@postech.ac.kr

The X-ray PIV (particle image velocimetry) technique has been used as a non-invasive measurement modality to investigate the haemodynamic features of blood flow. However, the extraction of two-dimensional velocity field data from the three-dimensional volumetric information contained in X-ray images is technically unclear. In this study, a new two-dimensional velocity field extraction technique is proposed to overcome technological limitations. To resolve the problem of finding a correction coefficient, the velocity field information obtained by X-ray PIV and micro-PIV techniques for disturbed flow in a concentric stenosis with 50% severity was quantitatively compared. Micro-PIV experiments were conducted for single-plane and summation images, which provide similar positional information of particles as X-ray images. The correction coefficient was obtained by establishing the relationship between velocity data obtained from summation images (V_S) and centre-plane images (V_C). The velocity differences between V_S and V_C along the vertical and horizontal directions were quantitatively analysed as a function of the geometric angle of the test model for applying the present two-dimensional velocity field extraction technique to a conduit of arbitrary geometry. Finally, the two-dimensional velocity field information at arbitrary positions could be successfully extracted from X-ray images by using the correction coefficient and several velocity parameters derived from V_S.

1. Introduction

The X-ray PIV (particle image velocimetry) technique, which combines the advantages of X-ray imaging and the conventional PIV technique, was developed to investigate the biofluid phenomena of living organisms (Lee & Kim, 2003). Numerous other non-invasive measurement techniques, such as magnetic resonance imaging (Markl et al., 2010; Lorenz et al., 2014) and echocardiography (Kheradvar et al., 2010), have been developed to investigate biological flows in living organisms. However, they have their own intrinsic limitations (Jung et al., 2013). Compared with other non-invasive measurement techniques, the X-ray PIV technique has advantages in terms of spatial and temporal resolutions (Jung et al., 2013). Moreover, the temporal resolution of the X-ray PIV technique has been gradually increased by attaching an image intensifier and enhancing image quality (Jung et al., 2013). Therefore, the Reynolds number of measurable flows has also steadily increased (Jamison et al., 2011).

Among the numerous applicable research fields, the X-ray PIV technique has been particularly used to measure velocity field information of blood flows inside opaque tubes (Jung et al., 2013; Lee et al., 2014) and blood vessels (Park, Yeom & Lee, 2016). Velocity field measurements of blood flows are
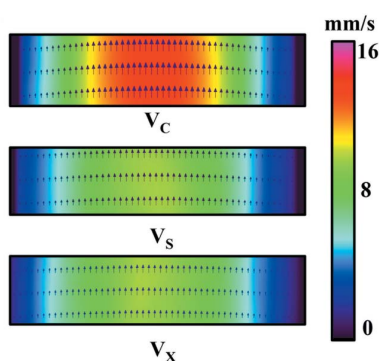
particularly important because wall shear stress (WSS) can be accurately evaluated from the velocity field information in the near-wall region. Abnormal blood flows with low WSS and oscillatory WSS are known as the main factors of cardiovascular diseases (CVDs) (Hove *et al.*, 2003). Pressure drop in blood vessels is another important factor that could be estimated by using the related velocity field information (Berger & Jou, 2000; Van Oudheusden, 2013). Therefore, the *in vivo* measurement of the near-wall velocity field of blood flows is crucial for understanding haemodynamic characteristics and early diagnosis of CVDs.

Disturbed flows in blood vessels may affect vascular endothelia (Chiu & Chien, 2011). Among the various vasculatures with disturbed flows, stenoses have been widely studied (Berger & Jou, 2000; Ku, 1997). A number of experimental and simulation studies have already been conducted. However, the exact haemodynamic mechanism has yet to be revealed, owing to several parameters, such as cells, proteins and plasma being closely associated in the progress of stenosis. In this case, *in vivo* experimental data are essential to examine the haemodynamic features in the stenosis. Recently, velocity field information on blood flows in the region of various stenoses was quantitatively measured under *in vitro*, *ex vivo* and *in vivo* conditions by adopting the X-ray PIV technique (Jamison *et al.*, 2011; Park, Yeom & Lee, 2016).

Although the performance of the X-ray PIV technique has gradually improved over a decade, several problems remain in the research on stenotic blood flows. One problem is the acquisition of amassed velocity field information. Each X-ray image contains all information of tracer particles located in the pathway of X-ray propagation, and the velocity field is obtained from positional information of these particles by using the X-ray PIV technique. Various velocity vectors along the X-ray pathway are accumulated in each interrogation window of the captured X-ray images. Therefore, the amassed velocity theory and peak smearing technique were used to extract two-dimensional velocity field information from the three-dimensional volumetric information contained in X-ray images (Lee & Kim, 2003; Fouras *et al.*, 2007). The amassed velocity theory for X-ray PIV measurement was expressed using the Navier–Stokes equation and Poiseuille's law. It was modified for application to shear thinning flows and this procedure is explained in detail in our previous studies (Lee & Kim, 2003; Lee *et al.*, 2014). However, the amassed velocity theory is difficult to apply for non-circular pipe flows, such as stenotic flow, because the amassed velocity equation was derived for the Poiseuille flow. Actually the flow characteristics in the stenosis region are quite different from those in a circular straight pipe. Thus, the velocity field information along the X-ray propagation is greatly influenced by the amassed positional information of tracer particles (Park, Park & Lee, 2016). Therefore, empirical and theoretical analyses are needed to accurately extract two-dimensional velocity field information of flows around various stenoses.

The main object of this study is to technically verify the measurement accuracy of the X-ray PIV technique by comparing it with the micro-PIV technique and to find a correction coefficient that can be used to extract two-dimensional velocity field information more accurately for various fluid flows in relatively complex geometries. Flows in a circular pipe and a concentric stenosis were tested in this study. First, the technical verification of the X-ray PIV technique was conducted by comparing the measured velocity field information with that obtained by the micro-PIV technique. The X-ray and summation images obtained by microscopy exhibit similar positional information of particles, because they contain all particles positioned in the pathway of beam propagation. This comparison with the micro-PIV technique ensures the legitimacy and usefulness of the X-ray PIV technique. The measurement accuracies of velocity field and WSS were also evaluated. Second, to extract two-dimensional velocity field information more accurately, correction coefficients were derived from the relationship between velocity information obtained by summation images (V_S) and centre-plane images (V_C). Two-dimensional velocity information can be extracted by applying the correction coefficient to the measured X-ray PIV results. Finally, the quantitative relationship between velocity components and geometrical parameters was derived for applying the X-ray PIV technique to conduits of arbitrary geometries.

2. Materials and methods

2.1. Comparison of X-ray PIV and micro-PIV techniques

Fig. 1 shows the experimental procedures to generate summation images I_S for PIV analysis. The summation image I_S is defined as

$$I_S(i, j) = \max\left[I_k(i, j), k = 1, 2, 3, \ldots, n\right], \qquad (1)$$

where $I_k(i, j)$ obtained by applying thresholding and band-pass filtering procedures (Zheng & Silber-Li, 2008) is the particle image on a two-dimensional plane (i, j). Particle images $I_k(i, j)$ were consecutively captured by moving the mechanical stage holding a microscope. The experimental procedure of this study is as follows:

(i) Identify the similarity of X-ray and summation images by comparing the corresponding velocity information obtained through X-ray images (V_X) and V_S.

(ii) Confirm the relationship between images $I_S(i, j)$ and $I_k(i, j)$, where k is an arbitrary number.

(iii) Find correction coefficients for every $I_k(i, j)$ and apply them to X-ray PIV results.

(iv) Find the specific relationship between the given geometrical configuration and velocity information to apply the X-ray technique to a conduit of arbitrary shape.

2.2. Stenosis model

The stenosis model with 50% severity and a circular pipe model were tested in this study. Fig. 2(*a*) depicts the geometrical parameters of the stenosis used in this study. The inner radius $y(x)$ of the stenosis can be expressed by the following equation (Ahmed & Giddens, 1983):
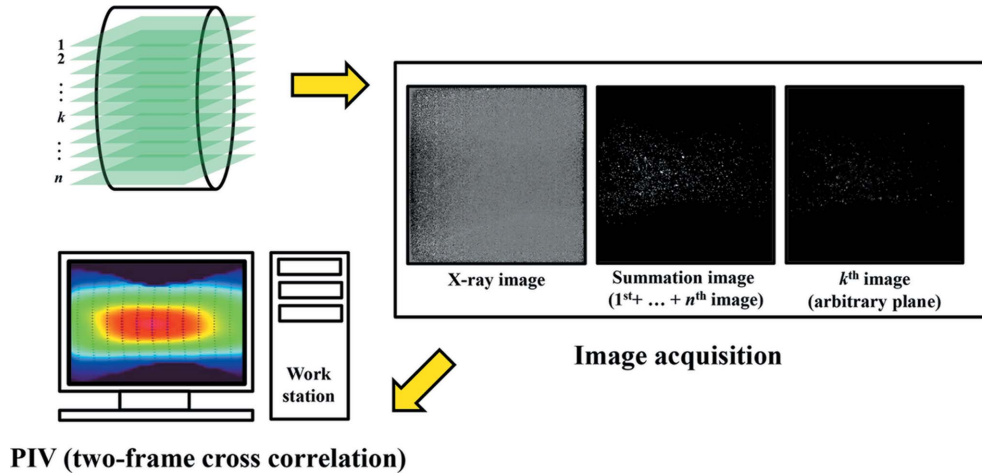
Figure 1
Experimental procedure to generate summation images used for comparison of V_S, V_C and V_X.
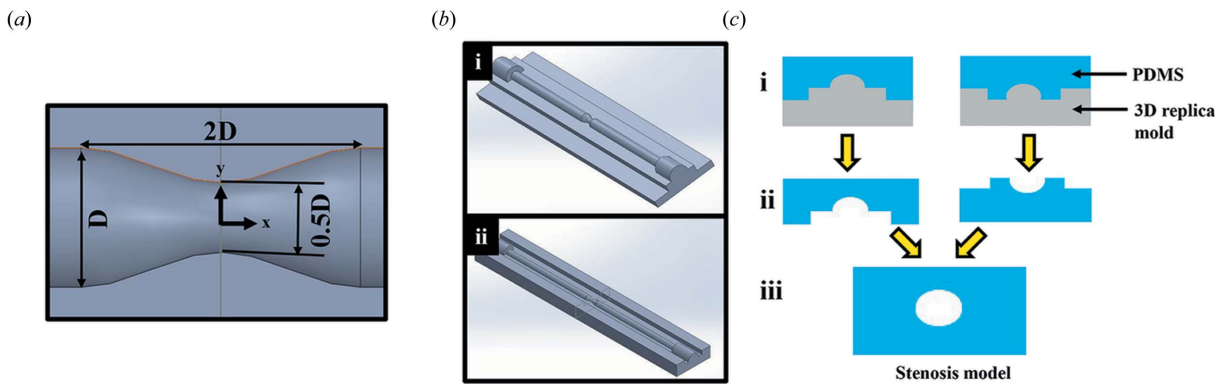
Figure 2
(*a*) Geometric parameters of the concentric stenosis model with 50% severity. (*b*) Illustration of three-dimensional stenosis moulds (i upper, ii lower) to fabricate the PDMS stenosis model. (*c*) Fabrication procedure of a three-dimensional PDMS stenosis model.

$$\frac{2y(x)}{D} = 1 - \delta\left[1 + \cos\left(\frac{x\pi}{D}\right)\right], \quad -D \le x \le D, \quad (2)$$

where D is the inner diameter of the stenosis and the corresponding value in the physical domain is 1.5 mm. The vessel blockage ratio of this stenosis clip is $\delta = 0.25$.

The upper and lower parts of the stenosis mould were fabricated separately with a three-dimensional printer (ProJet 3510 HDPlus, USA). The laminating thickness of the stenosis model was 16 μm (Fig. 2*b*). Fig. 2(*c*) shows the fabrication procedure of a three-dimensional polydimethylsiloxane (PDMS) stenosis model. The three-dimensional concentric stenosis channel with 50% severity and the circular pipe were made from PDMS. After pouring PDMS (Sylgard 184, Dow Corning, USA) into the upper and lower three-dimensional replica moulds, PDMS was cured at 313 K for 6 h. After the PDMS blocks were peeled from the three-dimensional replica moulds, the blocks were attached using oxygen plasma (CUTE, Femto Science, Korea) and instant glue. Silicon tubes (inner diameter = 1.5 mm, external diameter = 3 mm) were connected to both ends of the stenosis model. The microfluidic device was finally prepared by attaching the stenosis model to the glass substrate.

2.3. Microscopic imaging

Fig. 3(*a*) shows a schematic of the experimental setup of the micro-PIV measurement. A continuous laser (Shanghai Dream Laser Technology, Ltd, China) of 1 W was used in this study to excite fluorescence particles. Two plano-convex lenses with focal lengths of 250 and 50 mm were used to expand the beam. Tracer particles used in micro-PIV experiments were polymer fluorescent microspheres of 1 μm in average diameter (Duke Scientific Corporation, CA, USA). For acquiring $I_k(i, j)$, the narrow focal plane was formed by using a 10× objective lens with a numerical aperture (NA) of 0.45. Focal plane thickness influences the depth of correlation (δz_{corr}), which is highly related to particle images (Nguyen *et al.*, 2010). δz_{corr} was calculated as follows (Olsen & Adrian, 2000):

$$\delta z_{corr} = 2\left[\frac{1 - \varepsilon^{1/2}}{\varepsilon^{1/2}}\left(\frac{d_p^2}{4NA^2} + \frac{5.95(M+1)^2\lambda^2}{16M^4 NA^4}\right)\right]^{1/2}, \quad (3)$$

where ε is the signal threshold at the ends of δz_{corr}, M is the lens magnification and λ is the fluorescent wavelength. The distance between two planes is 70 μm, which is larger than δz_{corr}. A Notch filter of 532 nm was utilized to block the
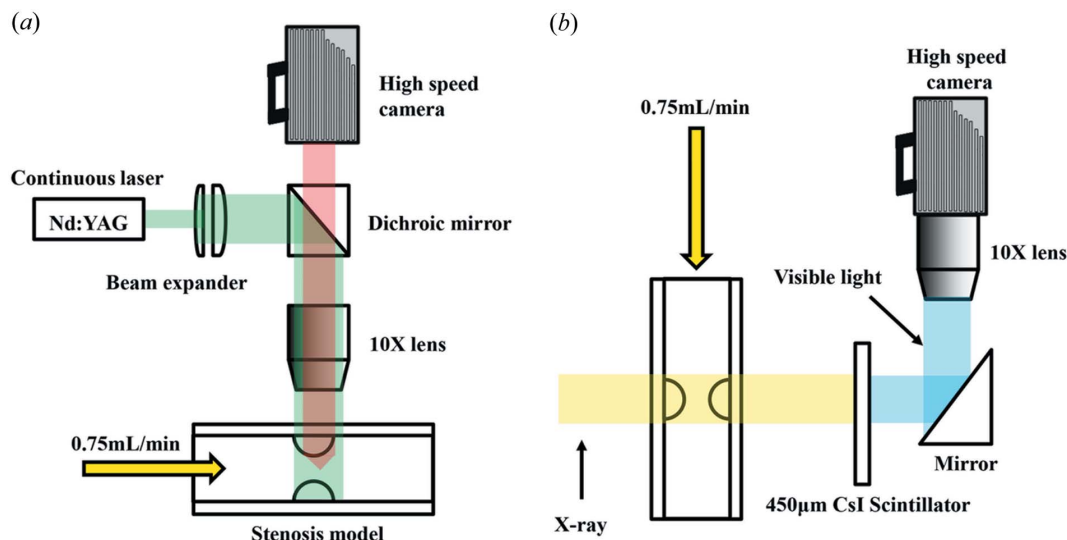
Figure 3
Experimental setup for (*a*) micro-PIV and (*b*) X-ray PIV measurements.

backscattering of green light. Images were consecutively captured by a high-speed camera (SA 1.1, Photron, Japan) at 1000 frames per second for 0.5 s. The field of view was 1945 × 1945 μm (1024 × 1024 pixels). The background elimination technique and thresholding method were used in this study to remove out-focused particle images.

2.4. X-ray PIV and image processing

Fig. 3(*b*) shows the experimental setup for X-ray PIV measurement. The experiments were conducted at the 6C Biomedical Imaging Beamline (6C BMI) of Pohang Light Source II (PLS-II). The beam current was 360 mA and the storage energy was 3 GeV. A monochromatic X-ray with beam flux of 1.2×10^{12} photon s^{-1} mm^{-1} was used. The X-ray passing through a 1 mm-thickness silicon wafer was 24 keV. The X-ray size was 8 mm (H) × 5 mm (V). The test model was positioned at approximately 30 m downstream from the X-ray source. A CsI scintillator of 450 μm in thickness was utilized as the scintillator crystal. The distance between the scintillator and the test model was fixed at 50 cm. X-ray images were consecutively recorded with the high-speed camera used in the micro-PIV experiments. The 10× objective lens was also utilized in the X-ray PIV experiments, and the image acquisition conditions were identical to those used for the micro-PIV experiments.

The flat-field correction method was used to minimize inhomogeneous beam illumination and a spatial frequency filter was used to reduce beam fluctuations (Jung *et al.*, 2013). Silver-coated hollow glass particles with diameters of 14 μm were used as tracer particles.

2.5. Experimental conditions and PIV analysis

A working fluid mimicking blood was used in this study. The preparation of this working fluid is described in our previous study (Ha & Lee, 2014). The working fluid is composed of 44%

glycerol and 56% deionized water. Sodium iodine was utilized to match the reflective index of PDMS with that of the working fluid (1.4130 ± 0.0005).

The experimental models and experimental conditions were the same for both X-ray PIV and micro-PIV experiments. The working fluid was supplied by a syringe pump (PHD 2000, Harvard Apparatus, USA) at a flow rate of 0.75 ml min^{-1}. The two-frame cross-correlation algorithm was used to calculate the velocities V_S, V_C and V_X. 400 consecutive velocity field values were ensemble-averaged to obtain time-averaged mean flow information. The interrogation window size was 64 pixel (horizontal) × 32 pixel (vertical) with 50% overlapping.

3. Results and discussion

3.1. Velocity information in Poiseuille flow

Recently, disorders in circulatory vasculatures, such as stenoses (Carabello, 2013) and vulnerable plaques (Slager *et al.*, 2005; Naghavi *et al.*, 2003), are among the major causes of mortality. Therefore, detailed studies on the mechanism of CVDs and early diagnosis of CVDs are essential and urgent. Several non-invasive measurement techniques have been developed to investigate the haemodynamic features of CVDs under *in vivo* or *ex vivo* conditions. Among these techniques, the X-ray PIV technique with high spatial and temporal resolution has been used. However, owing to the technical limitations encountered in the extraction of two-dimensional velocity information, X-ray PIV has been mainly applied to haemodynamic studies on simple geometries, such as a straight pipe. Exceptional applications are limited to simple stenosis (Jamison *et al.*, 2011; Park, Park & Lee, 2016) and aneurysm (Yang *et al.*, 2017). Therefore, the accurate extraction of two-dimensional velocity field information from three-dimensional volumetric information contained in X-ray images is challenging for applying the X-ray PIV technique to CVD research.

In this study, a new two-dimensional velocity field extraction technique is proposed, and its measurement accuracy demonstrated by comparison with the results of the micro-PIV technique, which is accepted as a reliable velocity field measurement method (Nguyen *et al.*, 2010; Kloosterman *et al.*, 2011; Poelma *et al.*, 2012; Lindken *et al.*, 2009). First, the velocity field of the Poiseuille flow was measured using X-ray PIV and micro-PIV techniques. The velocity field information of the Poiseuille flow in a circular pipe was measured by a combination of X-ray PIV and micro-PIV techniques. The Stokes numbers of 1 μm polymer fluorescent microspheres and 14 μm silver-coated hollow glass spheres are 1.03×10^{-4} and 3.07×10^{-3}, respectively. When the Stokes number is much less than 0.1, the tracing error is below 1% (Tropea & Yarin, 2007). Thus, velocity information obtained by the two tracer particles was directly compared in this study. Fig. 4(a) shows a comparison between the time-averaged mean velocity fields of a Poiseuille flow measured by both techniques. The maximum centre-plane velocity of V_C was 14.15 mm s^{-1} and the corresponding Reynolds number was 5.48 based on the physical properties of the working fluid, namely, dynamic viscosity of 4.3×10^{-3} kg m^{-1} s^{-1} and density of 1110 kg m^{-3}. The calculated flow rate based on the maximum velocity of V_C was 0.75 ml min^{-1}. Fig. 4(b) shows variations in the streamwise mean V_C, V_S and V_X of the Poiseuille flow along the radial direction. The magnitudes of amassed velocities were approximately two-thirds of the theoretical values of the Poiseuille flow (Lee & Kim, 2003). All velocity components were normalized by the maximum V_C. In this study, a working fluid mimicking blood was used. Its dynamic viscosity was about 4.30 ± 0.05 cP, which is within the range of human blood viscosity (4.4 ± 0.6 cP) (Yousif *et al.*, 2009). Because the working fluid used in this study is a Newtonian fluid, viscous flow behaviours are manifested in the stenosed channel. Although the viscosity of whole blood varies according to share rate due to aggregation of red blood cells, the dynamic viscosity of the blood-mimicking working fluid is well matched with that of whole blood under the present experimental conditions. Since the haemodynamic behaviours of blood flows are important, the present X-ray PIV technique verified in this study would be helpful for obtaining haemodynamic
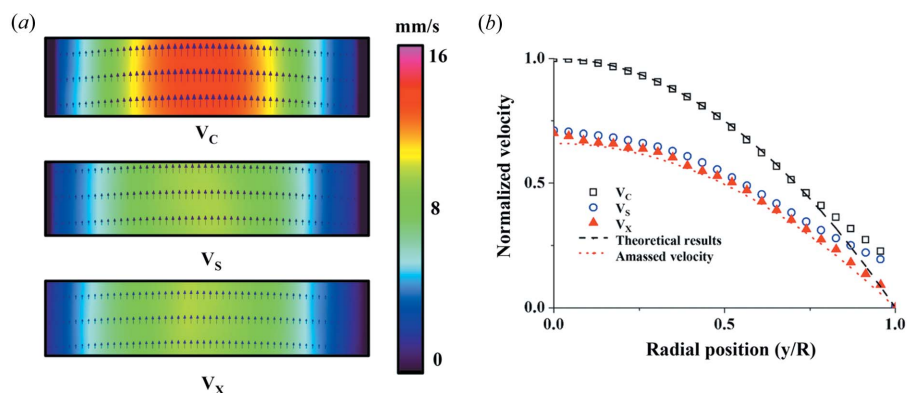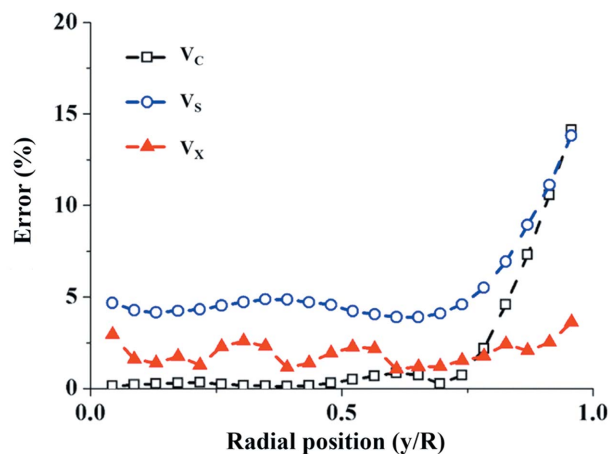
Figure 5
Variations of measurement errors of V_C, V_S and V_X of a Poiseuille flow along the radial direction.

information of opaque blood flows in various disease models under various flow conditions.

Fig. 5 shows the error variations in the measured V_C, V_S and V_X along the radial direction. Here, the error denotes the difference between experimental and theoretical results. In X-ray PIV measurements, the velocity differences are less than 5% at all radial positions. In contrast, the differences of V_S and V_C are dramatically increased on approaching the near-wall region due to the augmenting effect of δz_{corr} (Nguyen *et al.*, 2010). As δz_{corr} increases, the velocity magnitude increases in the near-wall region. Therefore, the measurement accuracy of V_S and V_C decreased in the near-wall region. The peak heights and peak widths in the cross-correlation map are different in the centre and near-wall regions because of different intensities of particle images in the focal plane. By contrast, regardless of radial position, the image intensities of particles are nearly constant in the X-ray images. Although inhomogeneous X-ray illumination would give rise to slightly different intensity values, the employed flat-field correction procedure removes the effect of inhomogeneous beam illumination. Therefore, the measurement accuracy of X-ray PIV was constant throughout the radial direction. Given that WSS is derived from the velocity gradient in the near-wall region, the X-ray PIV technique, which provides higher measurement accuracy in the near-wall region, would provide better results in WSS measurement.

3.2. Velocity information of flow in the 50% concentric stenosis

Velocity field information of the working fluid in the concentric stenosis with 50% severity was measured by using the X-ray PIV and micro-PIV techniques. Fig. 6(a) shows variations in the normalized centreline V_C, V_S and V_X according to velocity measurement

Figure 4
(a) Mean velocity fields obtained from the centre-plane, summation and X-ray images of a Poiseuille flow. (b) Comparison of normalized mean velocity profiles.

manner. The time-averaging scheme was adopted for each velocity component, which was normalized by the maximum V_X (centreline velocity at $x/D = 0$). The maximum velocity measured from X-ray images was 23.29 mm s^{-1}. V_X, V_C and V_S have maximum values at the crest of the stenosis. The normalized centreline velocities decreased as x/D increased. The inset in Fig. 6(a) shows variations in the correction coefficient, which is defined as the ratio V_S/V_C. Different from the constant value (2/3) for the Poiseuille flow, the correction coefficient gradually decreased as x/D increased. Fig. 6(b) shows a comparison of the variations in the normalized V_S and V_X with respect to radial position. The maximum velocity and velocity gradient in the near-wall region decreased as x/D increased. The average differences between V_X and V_S in the 50% concentric stenosis are 3.74%, 2.82% and 3.55% at axial positions of $x/D = 0$, 0.25 and 0.5, respectively. Except in the near-wall region, the velocity information of V_X and V_S is well matched in both the Poiseuille flow and disturbed flow in the stenosis with 50% severity. The velocity differences in the near-wall region became significant at small velocity magnitudes (Nguyen *et al.*, 2010). Therefore, the velocity differences are smaller in the near-wall region of the 50% stenosis compared with those in the Poiseuille flow because the velocities at the stenosis are faster than those of the Poiseuille flow.


(a)

(b)
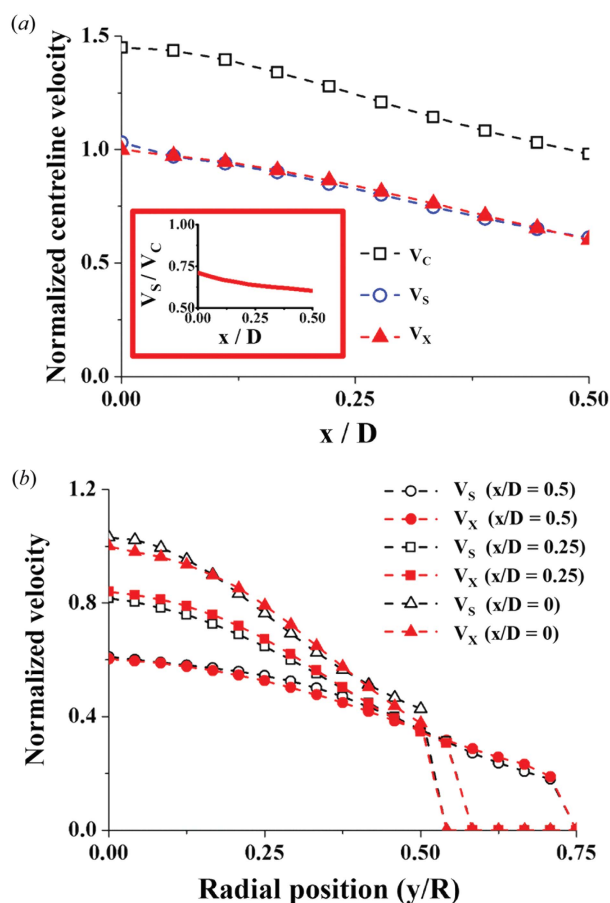
Figure 6
(a) Variations of the normalized centreline velocities V_C, V_S and V_X along the axial direction. Inset represents the ratio of V_S to V_C. (b) Comparison of radial variations of normalized velocities V_X and V_S.

The summation image $I_S(i, j)$ is composed of particle images captured in a two-dimensional plane $I_k(i, j)$ ($k = 1, 2, \ldots, n$) and the corresponding distance between adjacent particle images is 70 µm. Therefore, the velocity information along the depthwise direction [y direction in Fig. 2(a)] was discretely obtained with intervals of 70 µm. The interval of 70 µm was determined based on the depth-of-focus of the objective lens used in this study. On the other hand, the velocity information obtained from X-ray images is composed of all velocity information along the pathway of X-ray propagation. In the throat of the stenosis, the velocity profile has a jet-like shape and high-speed velocity components are dominant along the depth direction. Because only high-speed velocity components are expressed in the micro-PIV results, low-velocity information in the near-wall region is omitted due to the interval of 70 µm in the depthwise direction. On the other hand, because all velocity information is continuously expressed in the X-ray PIV results, the low velocity of V_X is relatively larger than V_S. Therefore, V_X is smaller than V_S in the stenotic throat at $x/D = 0$, because much low-velocity information was averaged. As x/D increases, the velocity profile along the y direction becomes blunt. Therefore, the omission of low-velocity information is decreased and the resultant differences between V_S and V_X are decreased on going downstream from the throat. If the interval between adjacent two-dimensional particle images is reduced, the difference between V_S and V_X would be decreased.

3.3. Determination of correction coefficient

Correction coefficients used for amassed velocities were obtained from the ratio of velocity field information derived from summation and arbitrary plane images. For applying the correction coefficient to stenoses of various severities, variations in velocity components were analysed according to the geometric angle (GA) of the test model. First, the variations in GA were compared with those of velocity angles obtained from the centre plane (VA$_C$) and summation images (VA$_S$). The velocity angle (VA) was derived using the formula $\tan^{-1}(V_y/U_x)$, where U_x and V_y are the velocity components in the x and y directions, respectively. GAs were acquired from each point at which velocity vectors were obtained. Fig. 7(a) shows the variation of GA according to VA$_C$. The coefficient of determination (R^2) is 0.9822 and the corresponding equation (red dashed line) is expressed as GA = 0.83 VA$_C$. Fig. 7(b) shows the relationship between VA$_C$ and VA$_S$. The R^2 value is 0.9696 and the corresponding slope (red dashed line) is VA$_S$ = VA$_C$. These results support the observation that the parameters GA, VA$_S$ and VA$_C$ show linear relationships and that the estimation of GA using VA is reasonable. The linear relationship between GA and VA$_S$ is important because the VA$_S$ values can be directly acquired from the measured velocity field data without geometrical information on the test conduit. Therefore, the analysis of velocity differences is possible by using the measured VA$_S$ data instead of GA.

The variations in velocity differences in the vertical (V) and horizontal (H) directions with respect to velocity angle are

(a)

(b)
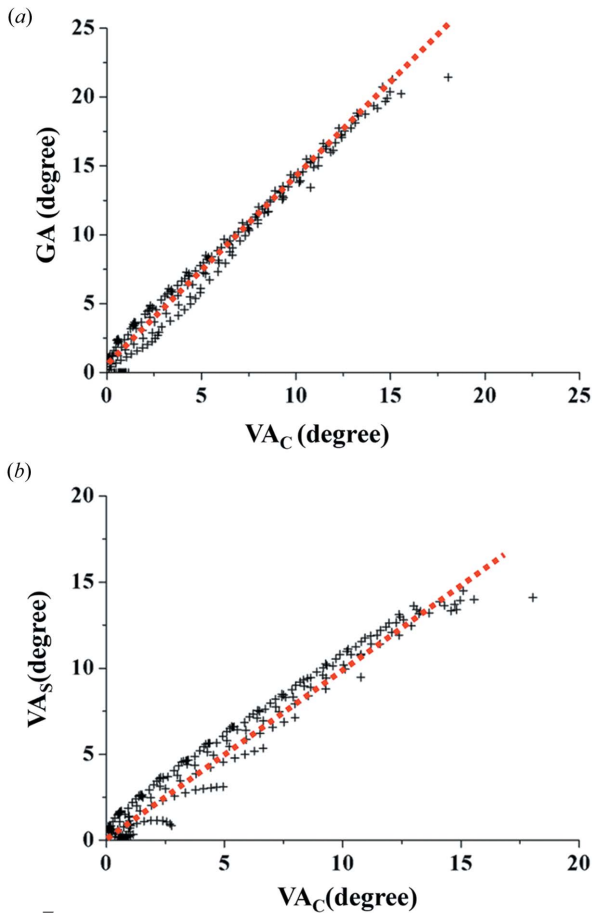
Figure 7
(a) Scatter plot of GA according to VA_C. (b) Scatter plot of VA_S according to VA_C.

illustrated in Figs. 8(a) and 8(b). Here, the velocity difference is defined as $(V_C - V_S)/V_C$. Therefore, the correction coefficients can be obtained by subtracting the velocity differences from 1. Fig. 8(a) shows a scatter plot of the velocity differences in the horizontal direction (ΔU) according to velocity angle VA_S. The red dashed line indicates the data at $x/D = 0.25$. The upper part of this dashed line represents the radial positions $x/D > 0.25$. The variations of ΔU with respect to VA_S increased as x/D decreased. Fig. 8(b) shows a scatter plot of the velocity differences in the vertical direction (ΔV) according to velocity angle VA_S. Most dots in the scatter plots are distributed along the red dashed line derived by using the fourth-order curve fitting. The fitting curve is expressed by $\Delta V = 0.011\,VA_S^4 - 0.368\,VA_S^3 + 3.736\,VA_S^2 - 10.799\,VA_S + 14.903$, and the corresponding R^2 value is 0.6881. The data in the blue triangle region are negligible because the vertical velocity component has very low values at low VA_S conditions (near the centreline). The correction coefficient in the vertical and horizontal directions can be estimated from Fig. 8. Thus, the velocity information at an arbitrary plane can be directly extracted by using the summation image velocity V_S and correction coefficient because the parameters x/D, VA_S, ΔU, ΔV and $\Delta U/\Delta VA_S$ are related to V_S.

WSS is one of the most important parameters to understand the haemodynamic characteristics of blood flows (Malek *et al.*,

1999), and both small and large variations in WSS have a strong influence on the occurrence of atherosclerosis (Millon *et al.*, 2015). In this study, the values of V_C were compared with those of V_S, and the corresponding correction coefficients were acquired. However, despite the identical stenosis shape, the WSS distributions are changed according to the given inlet flow conditions, such as swirling flow and anastomosis (Ha *et al.*, 2015). Moreover, given that most stenoses have complicated asymmetric shapes, accurate *in vivo* velocity measurement of blood flows is essential to understand the haemodynamic characteristics of blood flows in stenoses with complicated configuration shapes. Velocity field information including WSS in an arbitrary plane can also be measured by using the present X-ray PIV technique at all positions in the stenosis. The correction coefficients at any planes of the stenosis can be estimated based on the velocity data obtained from summation and arbitrary plane images. Thus, although a brief pre-experiment using a micro-PIV technique is needed to find the proper correction coefficients, the velocity field information of blood flows in the whole stenosis region with bifurcation or aneurysm can be obtained by using the present X-ray PIV technique which adopts correction coefficients.

The current problem of the X-ray PIV technique is its low temporal resolution. To resolve this problem, many efforts

(a)

(b)
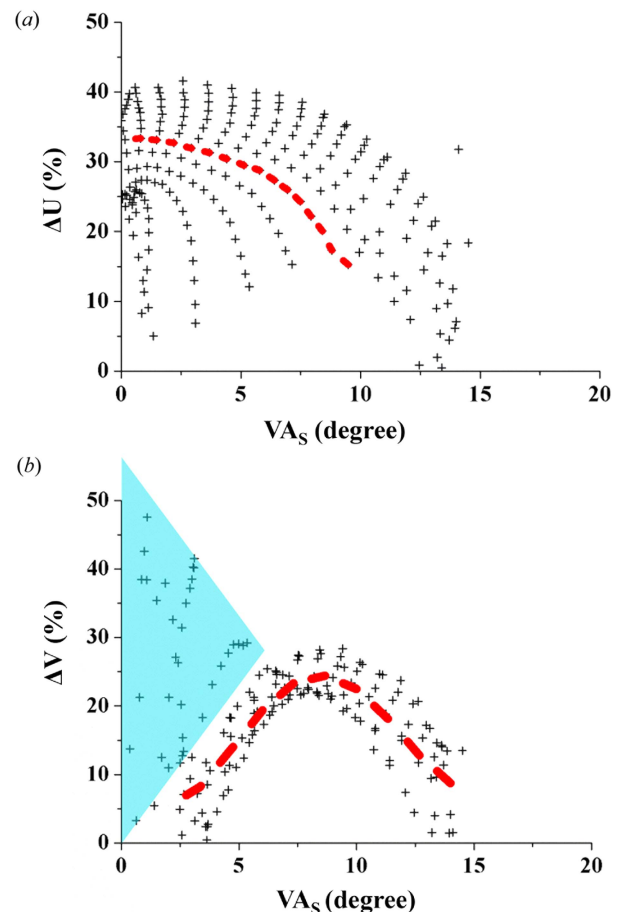
Figure 8
(a) Scatter plot of the horizontal velocity difference ΔU according to VA_S obtained from summation images. (b) Scatter plots of the vertical velocity difference ΔV according to VA_S obtained from summation images.

have been made such as the use of an image intensifier and high-speed X-ray CCD (Park, Yeom & Lee, 2016; Jamison *et al.*, 2012; Jung *et al.*, 2013). The use of an advanced X-ray source is another way to increase the temporal resolution of the X-ray PIV technique. Instead of monochromatic X-rays as used in this study, polychromatic X-rays might be an alternative way to increase the temporal resolution. Recently, X-ray velocimetry with the aid of an array X-ray source was developed to enhance temporal resolution (Gonzales *et al.*, 2014). Although several technical limitations remain, the present X-ray PIV technique demonstrates strong potential for the investigation of haemodynamic information and pathological characteristics in animal disease models.

4. Conclusion

Although the X-ray PIV technique has strong potential in the study of haemodynamic characteristics under *in vivo* and *ex vivo* conditions, its application is limited because of the technical difficulties encountered in two-dimensional velocity extraction. The direct comparison of the experimental data measured by the proposed X-ray PIV technique with those of the micro-PIV technique demonstrates the improved measurement performance. The proposed X-ray PIV could be applied to various stenoses with arbitrary shape. Moreover, X-ray PIV can measure WSS accurately in the near-wall region because of high measurement accuracy in the near-wall region. This study will be helpful in the use of the X-ray PIV technique for studying haemodynamic characteristics in animal disease models and biomedical applications.

References

Ahmed, S. A. & Giddens, D. P. (1983). *J. Biomech.* **16**, 505–516.
Berger, S. & Jou, L. D. (2000). *Annu. Rev. Fluid Mech.* **32**, 347–382.
Carabello, B. A. (2013). *Circ. Res.* **113**, 179–185.
Chiu, J. J. & Chien, S. (2011). *Physiol. Rev.* **91**, 327–387.
Fouras, A., Dusting, J., Lewis, R. & Hourigan, K. (2007). *J. Appl. Phys.* **102**, 064916.
Gonzales, B., Spronk, D., Cheng, Y., Tucker, A. W., Beckman, M., Zhou, O. & Lu, J. (2014). *IEEE Access*, **2**, 971–981.
Ha, H., Choi, W. & Lee, S. J. (2015). *Med. Eng. Phys.* **37**, 272–279.
Ha, H. & Lee, S. J. (2014). *Med. Eng. Phys.* **36**, 1106–1114.
Hove, J. R., Köster, R. W., Forouhar, A. S., Acevedo-Bolton, G., Fraser, S. E. & Gharib, M. (2003). *Nature (London)*, **421**, 172–177.
Jamison, R. A., Dubsky, S., Siu, K. K., Hourigan, K. & Fouras, A. (2011). *Ann. Biomed. Eng.* **39**, 1643–1653.
Jamison, R. A., Siu, K. K. W., Dubsky, S., Armitage, J. A. & Fouras, A. (2012). *J. Synchrotron Rad.* **19**, 1050–1055.
Jung, S. Y., Park, H. W., Kim, B. H. & Lee, S. J. (2013). *J. Synchrotron Rad.* **20**, 498–503.
Kheradvar, A., Houle, H., Pedrizzetti, G., Tonti, G., Belcik, T., Ashraf, M., Lindner, J. R., Gharib, M. & Sahn, D. (2010). *J. Am. Soc. Echocardiogr.* **23**, 86–94.
Kloosterman, A., Poelma, C. & Westerweel, J. (2011). *Exp. Fluids*, **50**, 1587–1599.
Ku, D. N. (1997). *Annu. Rev. Fluid Mech.* **29**, 399–434.
Lee, S. J. & Kim, G. B. (2003). *J. Appl. Phys.* **94**, 3620–3623.
Lee, S. J., Park, H. W. & Jung, S. Y. (2014). *J. Synchrotron Rad.* **21**, 1160–1166.
Lindken, R., Rossi, M., Grosse, S. & Westerweel, J. (2009). *Lab Chip*, **9**, 2551–2567.
Lorenz, R., Bock, J., Barker, A., von Knobelsdorff-Brenkenhoff, F., Wallis, W., Korvink, J., Bissell, M., Schulz-Menger, J. & Markl, M. (2014). *Magn. Reson. Med.* **71**, 1542–1553.
Malek, A. M., Alper, S. L. & Izumo, S. (1999). *J. Am. Med. Assoc.* **282**, 2035–2042.
Markl, M., Wegent, F., Zech, T., Bauer, S., Strecker, C., Schumacher, M., Weiller, C., Hennig, J. & Harloff, A. (2010). *Circ. Cardiovasc. Imaging*, **3**, 647–655.
Millon, A., Sigovan, M., Boussel, L., Mathevet, J. L., Louzier, V., Paquet, C., Geloen, A., Provost, N., Majd, Z., Patsouris, D., Serusclat, A. & Canet-Soulas, E. (2015). *PLoS One*, **10**, e0141880.
Naghavi, M. *et al.* (2003). *Circulation*, **108**, 1664–1672.
Nguyen, C. V., Fouras, A. & Carberry, J. (2010). *Exp. Fluids*, **49**, 701–712.
Olsen, M. & Adrian, R. (2000). *Exp. Fluids*, **29**, S166–S174.
Park, H., Park, J. H. & Lee, S. J. (2016). *Sci. Rep.* **6**, 37985.
Park, H., Yeom, E. & Lee, S. J. (2016). *Sci. Rep.* **6**, 19194.
Poelma, C., Kloosterman, A., Hierck, B. P. & Westerweel, J. (2012). *PLoS One*, **7**, e45247.
Slager, C., Wentzel, J., Gijsen, F., Schuurbiers, J., van der Wal, A., van der Steen, A. & Serruys, P. (2005). *Nat. Clin. Pract. Cardiovasc. Med.* **2**, 401–407.
Tropea, C. & Yarin, A. L. (2007). *Springer Handbook of Experimental Fluid Mechanics*. Springer Science and Business Media.
Van Oudheusden, B. (2013). *Meas. Sci. Technol.* **24**, 032001.
Yang, Z., Yu, H., Huang, G. P. & Ludwig, B. (2017). *J. Biomech. Eng.* **139**, 061005.
Yousif, M. Y., Holdsworth, D. W. & Poepping, T. L. (2009). *Engineering in Medicine and Biology Society 2009 (EMBC 2009), Annual International Conference of the IEEE*, pp. 1412–1415.
Zheng, X. & Silber-Li, Z. (2008). *Exp. Fluids*, **44**, 951–959.